



Evaluation of LPM permafrost distribution in NE Asia reconstructed and downscaled from GCM simulations

KAZUYUKI SAITO, SERGEI MARCHENKO, VLADIMIR ROMANOVSKY, AMY HENDRICKS, NANCY BIGELOW, KENJI YOSHIKAWA AND JOHN WALSH

BOREAS



Saito, K., Marchenko, S., Romanovsky, V., Hendricks, A., Bigelow, N., Yoshikawa, K. & Walsh, J. 2014 (July): Evaluation of LPM permafrost distribution in NE Asia reconstructed and downscaled from GCM simulations. *Boreas*, Vol. 43, pp. 733–749. 10.1111/bor.12038. ISSN 0300-9483.

A high-resolution map of potential frozen ground distribution in NE Asia (90–150°E, 25–60°N) at the period of the Last Permafrost Maximum (LPM, *c.* 21 000 years ago) was dually reconstructed by means of a statistical classification using air freezing and thawing indices and a topographical downscaling using a digital relief model (ETOPO1). Background LPM climate data were derived from global climate model simulations of the Paleoclimate Model Intercomparison Project, Phase II (PMIP2). The reconstructed LPM map shows the southward shift of the southern limit of climate-driven permafrost by 400–1500 km, with the greatest advance in the western sector (90–110°E), encompassing an area from central Siberia to most of the Altai area. The advance of environmentally conditional permafrost and seasonally frozen ground was greatest in the eastern sector (110–150°E), with an average shift of about 450 km. The descent of the lower limit of LPM alpine permafrost was in the range of 400–800 m. A comparison of the reconstructed map with published literature shows that this method, simplistically constructed yet effectively recognizing seasonality, continentality and topography, captures local features better than more elaborate methods. The sensitivity examination of a constant atmospheric lapse rate shows that altitudes of 2000–5000 m a.s.l. were most sensitive, though with only a limited effect on overall LPM distribution.

Kazuyuki Saito (ksaito@jamstec.go.jp), Japan Agency for Marine-Earth Science and Technology, 3173-25 Showamachi, Kanazawaku, Yokohama City, Kanagawa, 236-0001, Japan and International Arctic Research Center, University of Alaska Fairbanks, 930 Koyukuk Drive, Fairbanks, 99775-7340, Alaska, USA; Amy Hendricks and John Walsh, International Arctic Research Center, University of Alaska Fairbanks, 930 Koyukuk Drive, Fairbanks, 99775-7340, Alaska, USA; Sergei Marchenko, Geophysical Institute, University of Alaska Fairbanks, 915 Koyukuk Drive, Fairbanks, 99775-7320, Alaska, USA; Vladimir Romanovsky, Geophysical Institute, University of Alaska Fairbanks, 915 Koyukuk Drive, Fairbanks, 99775-7320, Alaska, USA and Earth Cryosphere Institute, Tyumen, Russian Federation; Nancy Bigelow, Alaska Quaternary Center, University of Alaska Fairbanks, 900 Yukon Dr., Fairbanks, 99775-5940, Alaska, USA; Kenji Yoshikawa, Water and Environmental Research Center, University of Alaska Fairbanks, 306 Tanana Loop, Fairbanks, 99775-5860, Alaska, USA; received 29th January 2013, accepted 5th July 2013.

The nature and extent of the frozen ground in NE Asia (here defined as the area between 90–150°E in longitude and 25–60°N in latitude) is not well known (Vandenberghe *et al.* 2004, 2012) compared with other areas of Eurasia and northern North America (Washburn 1980; Rozenbaum & Shpolyanskaya 1998; Hubberten *et al.* 2004; French 2007). This is partly due to the sparse field data available in the region. Essentially, three approaches have been used to reconstruct the presence or absence of frozen ground in regions where direct observation or evidence is not available. These approaches are: (i) statistical, (ii) physical offline (standalone) and (iii) physical online (coupled).

The statistical approach uses surrogate variables – for example, climate variables such as temperatures and landforms – with which to associate the subsurface thermal regime of the location. Surface mean annual air temperature (MAAT) is commonly used (Washburn 1980; French 2007; Levvasseur *et al.* 2011; Matsuoka 2011; Boeckli *et al.* 2012; Gruber 2012). Different threshold values for different application areas and periods have also been proposed. For example, either –5°C or –6°C, as discussed by Washburn (1980) for the presence of continuous permafrost, or –8°C, as pro-

posed by Renssen & Vandenberghe (2003) and Vandenberghe *et al.* (2004). In China, Jin *et al.* (2000) refer to –6.5°C as the threshold for stable permafrost. Freezing and thawing indices have also been used to infer the type of frozen ground (Harris 1981, 1982; Anisimov & Nelson 1997; Saito *et al.* 2009). The advantages of these statistical methods are their simplicity and ease of computation and application (in terms of time, space and coding). Reconstruction procedures can be defined based on even partial or limited available information. By comparison, physical approaches require physically consistent sets of relationships in the form of mathematical equations. On the other hand, statistical approaches may lack physical justification or consistency of results. In addition, the applicability of the method itself may be limited, as relationships that are valid at one place and for one period of time are not necessarily applicable to another place and time because the assumptions or background conditions upon which the relationships were built may have changed. Nevertheless, when information is relatively abundant, sophisticated methods may be built and applied to the reconstruction of permafrost distribution at finer spatial resolution (e.g. Levvasseur *et al.* 2011).

The physical offline approach utilizes numerical models such as land process models or permafrost dynamics models. This approach incorporates related physical processes to compute subsurface behaviour. The forcing data are usually given at the top of the layer and may include, depending on the complexity of the processes implemented in the models, temperature, precipitation, snow amount (in either depth or water equivalence), incoming short- and long-wave radiation, surface wind, humidity and/or surface pressure. The complexity of models may vary (see the reviews by Riseborough *et al.* 2008; Saito *et al.* 2013a); simple ones compute only thermal equilibrium, whereas elaborate ones compute transient thermal and hydrological states. This approach can be applied to any place or period of time in order to compute physically consistent results, as long as the necessary parameters (e.g. soil type, porosity, thermal diffusivity) and forcing data are adequate to drive the model. The necessary computational resources are not as high as in the case of the physical online (coupled) approach described below.

Large-scale numerical modelling, such as in global climate models (GCMs) or Earth system models (ESMs), has enabled the online (coupled) approach to predict and estimate frozen-ground distribution and its changes in a physically consistent context. Land process models can be coupled to atmospheric (or coupled ocean–atmospheric) GCMs. Several attempts have already been made to compute the subsurface regime and its change using both GCMs (Renssen & Vandenberghe 2003; Lawrence & Slater 2005; Saito *et al.* 2007) and the Earth system models of intermediate complexity (EMICs; Roche *et al.* 2007; Vandenberghe *et al.* 2012). None have been entirely successful (e.g. Burn & Nelson 2006; Lawrence & Slater 2006). Shortcomings and problems are being addressed and models have seen constant improvement (Alexeev *et al.* 2007; Nicolsky *et al.* 2007; Saito 2008; Lawrence & Slater 2010). The historical evolution of permafrost in the Late Pleistocene and Holocene has also been simulated by numerical models for selected sites (Delisle 1998; Sueyoshi & Hamano 2003; Kitover *et al.* 2012).

Recent advances in numerical modelling now enable simulations of the past state of the global climate system. For example, Saito *et al.* (2009) attempted to estimate frozen-ground distribution by developing a statistical method for classifying frozen-ground type using freezing and thawing indices at the ground surface. That study presented empirical relationships based on present-day freezing and thawing indices and the International Permafrost Association map for permafrost distribution. These were then applied to Paleoclimate Model Intercomparison Project, Phase II (PMIP2) GCM outputs (Braconnot *et al.* 2007) for both the modern-day and 21 000 year BP. The resulting maps were reasonable for their large scale, despite their neglect of important factors such as snow, topography

and soil characteristics. However, the horizontal resolution of these maps, about 300 by 300 km, was too coarse for comparison with knowledge accumulated from field studies. This is a disadvantage of the online approach – that increases in horizontal resolution require increases in computing resources on quadratic or cubic orders.

In this paper, we produce maps of higher resolution for NE Asia, refine the previous statistical approach, and employ a simplistic topographic downscaling technique with a fine-scale digital relief model. We apply these techniques to simulations for the permafrost that existed at the time of the Last Glacial Maximum (LGM).

Methods

We used annual air freezing and thawing indices for the Northern Hemisphere at 25 by 25 km resolution (721 by 721 points) Equal-Area Scalable Earth Grid (EASE-Grid) data, provided by the US National Snow and Ice Data Center (NSIDC; Zhang *et al.* 2005; Frauenfeld *et al.* 2007). The freezing (thawing) index used is the cumulative daily temperature below (above) the freezing point (i.e., 0°C). Although these indices are generally based on daily values, we used indices derived from the monthly values. Considering that the cumulative index uses temperature values as an indicator of the energy input to the ground, the freezing index (in degree-days Celsius) was computed as:

$$I_f = \sum_i T_i FD_i, \quad (1)$$

where T_i is the mean air temperature (in °C) in the i th month ($i=7, \dots, 18$, running from July to June of the next year), and FD_i is the number of days in the month if T_i is below the freezing point (or 0 otherwise). Similarly, the thawing index (in degree-days Celsius) was computed as:

$$I_t = \sum_i T_i TD_i, \quad (2)$$

where T_i is the mean air temperature (in °C) in the i th month ($i=1, \dots, 12$, running from January to December), and TD_i is the number of days in the month if T_i is greater than the freezing point (or 0 otherwise). Frauenfeld *et al.* (2007) assessed the validity of monthly based, rather than daily based, freezing indices. They show that the relative error is less than 5% for most high-latitude land areas. This is applicable to northeast Asia north of about 40°N.

The ‘Circum-arctic map of permafrost and ground ice conditions’, compiled by the International Permafrost Association (IPA; Brown *et al.* 1997) on the same 25 by 25 km EASE-Grid provided by NSIDC (termed IPA map hereafter) was used to determine present-day

permafrost distribution. The map still has uncertainty in the zoning and boundaries of permafrost, especially in those areas that have scarce or no observation sites.

For digital topographic data, ETOPO1 (Amante & Eakins 2009) was used in this study (Fig. 1A). The horizontal resolution of the ETOPO1 data is 1 arc-minute (approximately 2 km in latitude). Other digital elevation models with higher resolutions are also avail-

able, for example GTOPO30 (United States Geological Survey 2002) and the updated SRTM30 (Farr *et al.* 2007). However, it was essential in this study that ocean bathymetry was included in the data, since sea level at the time of the LGM was lower than today. We used an offset of 127 m (Clark & Mix 2002; Milne & Mitrovica 2008) to derive land areas at the time of the LGM. We did not take glacial isostasy into account (Fig. 1B).

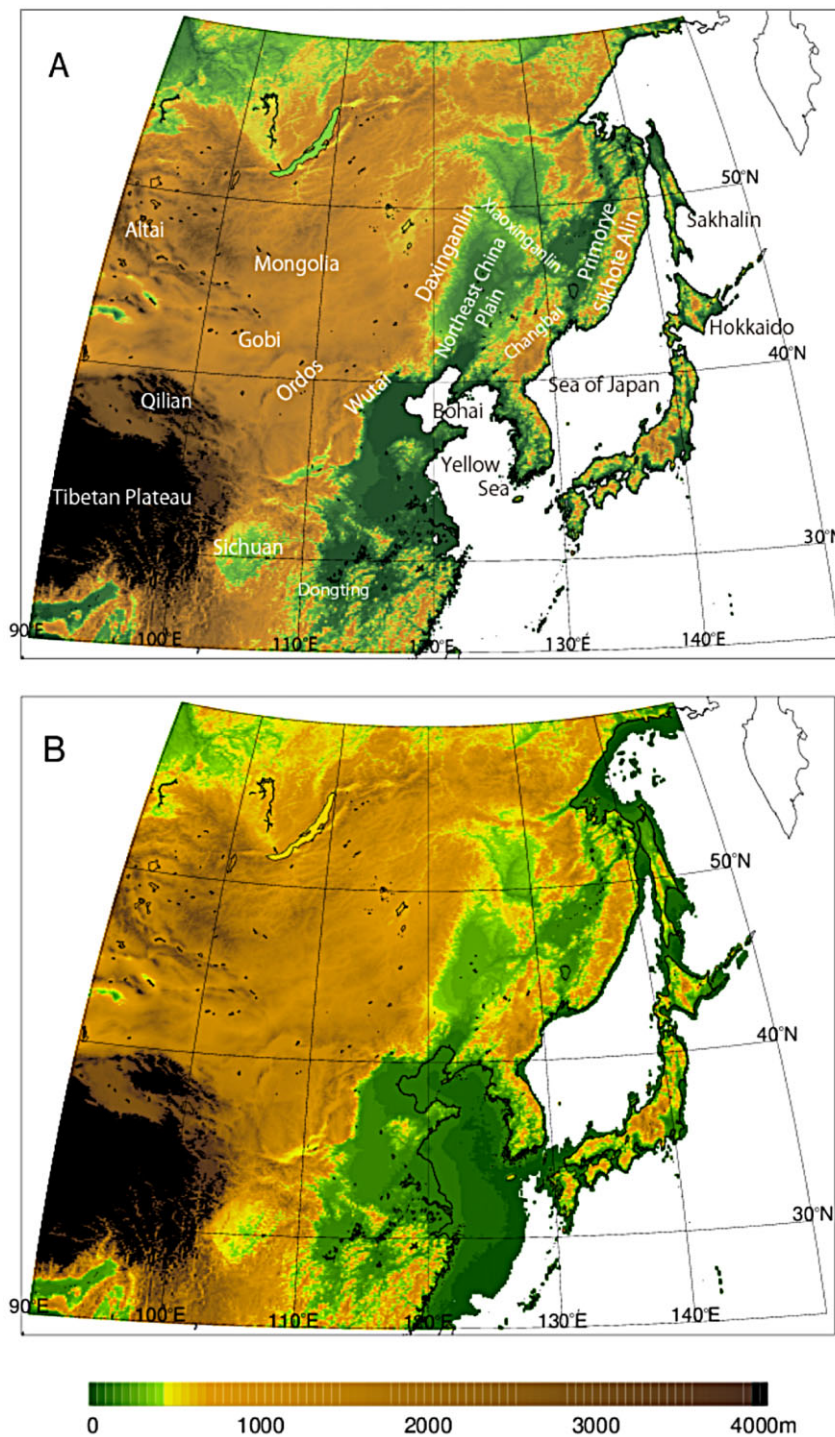


Fig. 1. Topography maps generated from ETOPO1 for the period of (A) the present day and (B) the LGM, which was uplifted equally by 127 m to account for the sea-level change. This figure is available in colour at <http://www.boreas.dk>

Table 1. List of the GCM simulations used in the study.

| Experiments/period | Pre-industrial (0 ka) | LPM (21 ka) |
|------------------------------------|--|--|
| Name of the models and simulations | CCSM (128x64; Collins <i>et al.</i> 2001), CNRM-CM33 (128x64; Salas-Méla <i>et al.</i> 2005), CSIRO-mk3L (64x56; Phipps 2006), ECHAM5-MPIOM1 (96x48; Roeckner <i>et al.</i> 2003), MIROC3.2 (128x64; Hasumi & Emori 2004), MIROC3.2.2 (128x64; Hasumi & Emori 2004), MRI-CGCM2.3.4fa (128x64, Yukimoto & Noda 2002), MRI-CGCM2.3.4nfa (128x64, Yukimoto & Noda 2002), UBRIS-HadCM3M2 (96x73, Gordon <i>et al.</i> 2000). | CCSM-mocat (128x64; Collins <i>et al.</i> 2001), CNRM-CM33 (128x64; Salas-Méla <i>et al.</i> 2005), HadCM3M2 (96x73, Gordon <i>et al.</i> 2000), IPSL-CM4-V1-MR (96x72, Marti <i>et al.</i> 2005), MIROC3.2 (128x64, Hasumi & Emori 2004), MIROC3.2.2 (128x64, Hasumi & Emori 2004). |

The GCM outputs, namely monthly surface air temperature at 2 m and orographic data, were obtained from the PMIP2 database (Braconnot *et al.* 2007). The archived PMIP2 data are complete and easily accessible. Simulations for 21 000 years BP were intended to examine climate at the time of the Last Glacial Maximum (LGM). However, in this paper we use the term Last Permafrost Maximum (LPM) to denote this period. Nine sets of numerical simulations were used for the pre-industrial control (0 ka), and six sets for the LPM. The models and simulations used in the study are summarized in Table 1.

Classification method

Harris (1981, 1982) was one of the first who used freezing and thawing indices to examine the relationship between permafrost distribution patterns for stations with snow accumulations of less than 50 cm (Fig. 2A). The advantage of using freezing and thawing indices rather than MAAT (which is also plotted by a set of thin lines for different values in Fig. 2A) is the ability to reflect seasonal change and continentality. The former is not necessarily symmetrical between warm and cool seasons; the latter is manifested by their amplitude. In fact, the limits of continuous (dash-dotted line) and sporadic (dotted line) permafrost proposed by Harris (1981) intersect the constant MAAT lines. This illustrates the difficulty and limitations of using MAAT alone as an indicator for inferring the subsurface thermal regime. The relationship derived by Saito *et al.* (2009) is also plotted by thick solid black lines on Fig. 2A. The difference between the data plotted by Harris (1981) and that of Saito *et al.* (2009) stems both from the fact that Harris used stations with relatively low snow cover, in order to exclude the insulation effects from the snow pack. By contrast, Saito *et al.* (2009) used freezing and thawing indices, derived at 25 by 25 km horizontal resolution, and matched these to permafrost types at the same scale. The primary objective was to utilize GCM surface temperature outputs for inference of the subsurface thermal regime at the representative area for each grid point. The entire area that was analysed consists of varying climatic and/or surface conditions. Snow-rich areas were included and

may have contributed to a shifting of the border lines determined by the surface air freezing index to the colder side in Fig. 2A. A set of blue lines is overlaid on Fig. 2A (Nelson & Outcalt 1987; Anisimov & Nelson 1997) to illustrate the use of (surface) freezing and thawing indices to classify regional and continental scale permafrost zones.

Frozen-ground classification

In an earlier study, Saito *et al.* (2009) recognized four types of frozen ground: 'permafrost', 'transitional', 'seasonal' and 'no frost'. In the present study we have attempted to capture the small-scale and short-term features that become apparent in high-resolution distribution. The revised classification formula (see below; also plotted in Fig. 2A by red lines) was constructed from subsets of the IPA map in contrast to Saito *et al.* (2009) who used the entire map. This is because a substantial part of the study area of NE Asia lacked direct temperature observations or geomorphological indicators. Therefore, we used only those grids that included borehole sites registered in the Global Terrestrial Network for Permafrost (GTN-P; <http://www.gtnp.org/>) inventory for the USA (92 grids; Fig. 2B), Russia (385 grids; Fig. 2C), China (42 grids; Fig. 2D) and Mongolia (52 grids; Fig. 2E). We assumed that the permafrost types at those grids in the IPA map reflected local conditions.

Equations are presented for two permafrost categories: (a) regions where the climatic condition favour the development and/or sustainment of continuous permafrost; (b) regions where the presence of permafrost is conditional upon environmental factors, such as ecosystem, topography or geology (Nelson *et al.* 2002; Shur & Jorgenson 2007). In addition, we divide seasonally frozen ground into two subcategories: (c) 'seasonal freezing' and (d) 'intermittent freezing' in order to distinguish between seasonal frost that is deep and/or lasting, and frost that exists for a short time (i.e., less than two weeks; Zhang *et al.* 2003). Finally, we consider the condition of no frost. In summary:

climate-driven permafrost (CP)

$$I_t < 0.9I_f - 2300; \quad (3)$$

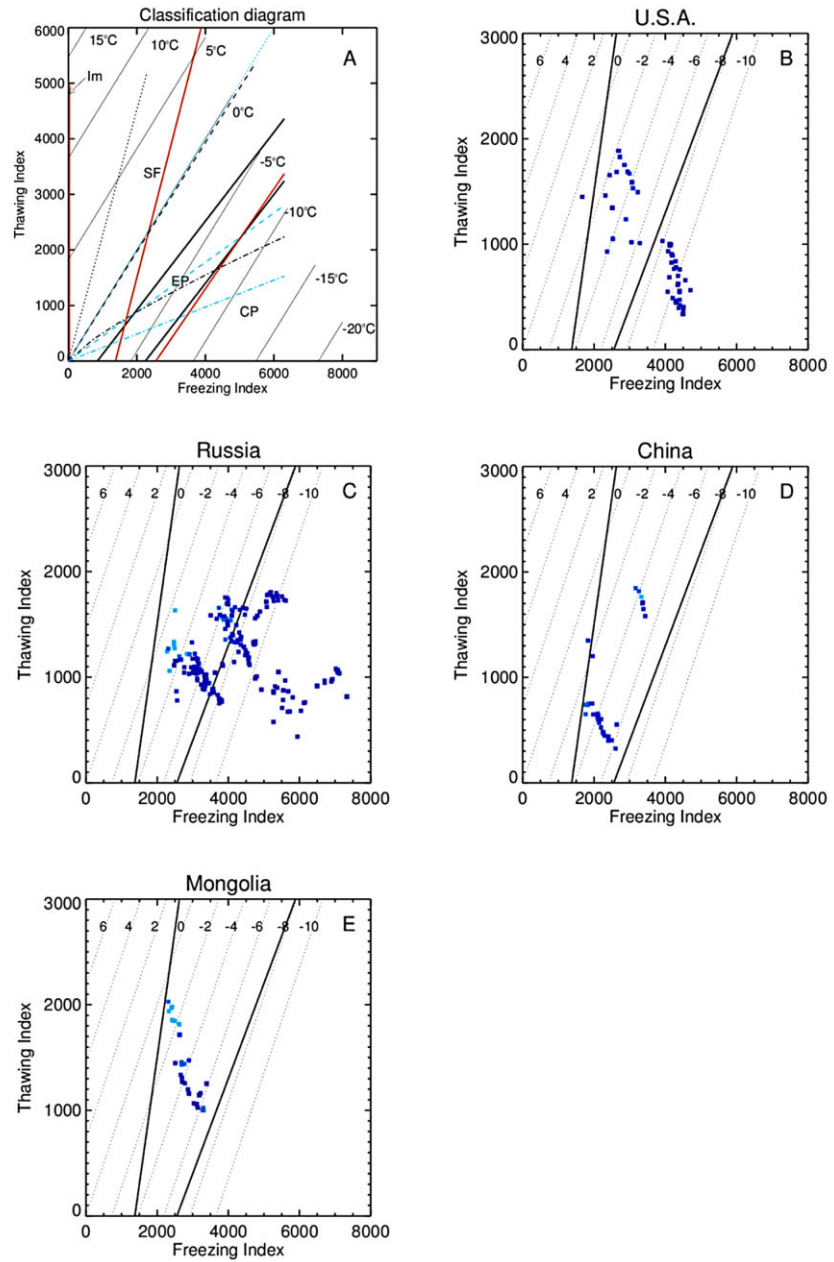


Fig. 2. A. Diagram of freezing and thawing indices, MAAT and frozen-ground type. MAAT at different values are shown by a set of thin lines. The classification proposed by Harris (1981) is shown by dot-dashed line for the limit of continuous permafrost, by dashed line for discontinuous permafrost and by dotted line for sporadic permafrost. The frost number method (Nelson & Outcalt 1987) is shown by the set of blue lines (dot-dashed for continuous permafrost, dashed for discontinuous and dotted for sporadic). Saito *et al.*'s (2009) results are shown by two thick black lines. This study's classification is shown by a set of red lines that dissect (from right to left) climate-driven permafrost (CP), environmentally conditional permafrost (EP), seasonal freezing (Sf) and intermittent freezing (Im). B. Examination of the permafrost classification undertaken by grids in the IPA map that include the borehole sites in the U.S.A. registered in the GTN-P inventory. C, D, E. Same as B except for Russia, China and Mongolia, respectively. This figure is available in colour at <http://www.boreas.dk>

environmentally conditional permafrost (EP)

$$0.9I_f - 2300 < I_t < 2.4I_f - 3300; \quad (4)$$

seasonally freezing (Sf)

$$2.4I_f - 3300 < I_t \text{ and } 30 < I_f; \quad (5)$$

intermittently freezing (Im)

$$0 < I_f \leq 30; \quad (6)$$

no freezing (Nf)

$$I_f = 0. \quad (7)$$

The high-resolution (i.e. same resolution as the ETOPO1 model) map of frozen-ground distribution was produced using the following procedures from the GCM outputs. Figure 3 illustrates an example of the process along the cross-section at 110°E latitude. The monthly air temperature at mean sea level (${}^{\text{model}}T_{\text{msl}}$) was calculated using the simulated surface air temperature (${}^{\text{model}}T_{\text{as}}$) and the GCMs' orographic data. The assumed atmospheric lapse rate (Γ) was a constant value of $6.5^\circ\text{C km}^{-1}$ (NOAA, 1976). Figure 3A compares simulated ${}^{\text{model}}T_{\text{as}}$ (thin solid lines) and calculated ${}^{\text{model}}T_{\text{msl}}$ (dashed lines) together against the observed T_{as} (thick solid line). Figure 3B shows the GCM orographic profiles (thin lines) used in the simulations

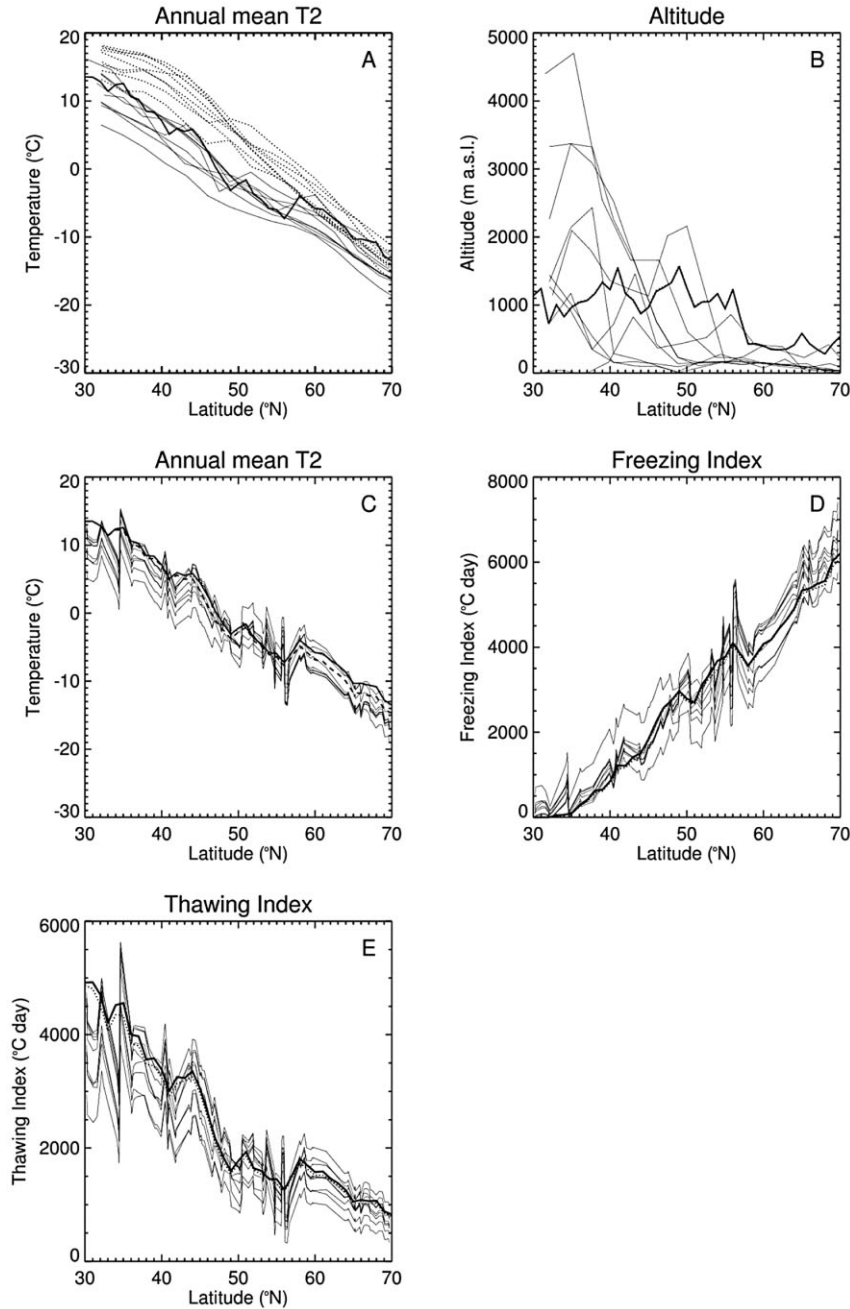


Fig. 3. Example of topographical downscaling of simulated surface air temperature along the latitude line of 110°E. Thick lines show observation-based data; thin lines show simulation-based variables. A. Mean annual air temperature. PMIP2 simulated surface air temperatures are shown by solid lines, and temperatures extrapolated to the mean sea level by dashed lines. B. Orography. Thick line is ETOPO1, while the GCM orography are shown by thin lines. C. Surface air temperature after interpolation (downscaling) into the ETOPO1 grids and conversion by the constant lapse rate Γ . D. Freezing indices. E. Thawing indices.

along 110°E, together with ETOPO1 orographic data (thick line). Note that the horizontal resolutions of GCM outputs (i.e. grid numbers for longitude and latitude) are different between models. For easy mutual comparison, calculated $T_{\text{msl}}^{\text{model}}$ values were first interpolated to a common grid system, for which we used a truncation level in the spectral space of T42 (at approximately 2.8° resolution – one of the finest resolutions among PMIP2 simulations). Interpolated $T_{\text{msl}}^{\text{T42}}$ was then further interpolated to the ETOPO1 (1 arc-minute) resolution, $T_{\text{msl}}^{\text{ETOPO1}}$. To ensure a smooth distribution of interpolated temperature, the value

($T_{\text{msl}}^{\text{ETOPO1}}(\mathbf{x})$ on an ETOPO1 grid, \mathbf{x}) was determined from values of the neighbouring 16 (i.e. 4 by 4) T42 grids, ξ_i ($i=1, 16$):

$$T_{\text{msl}}^{\text{ETOPO1}}(\mathbf{x}) = \left(\left(\sum_i d_i^{-2} \right)^{\text{T42}} T_{\text{msl}}(\xi_i) \right) / \left(\sum_i d_i^{-2} \right), \quad (8)$$

in which d_i is the distance between a T42 grid ξ_i and the ETOPO1 grid \mathbf{x} – namely, $(|\xi_i - \mathbf{x}|^2)^{1/2}$. Finally, the surface air temperature at the ETOPO1 grid, $T_{\text{as}}^{\text{ETOPO1}}(\mathbf{x})$, is computed with the ETOPO1 altitude – that is, $h(\mathbf{x})$ for 0 ka and $h(\mathbf{x}) + 127$ for LPM, and with the common lapse rate Γ (Fig. 3C). Finally, the annual

freezing index, I_f , and thawing index, I_t (in units of °C day³), were derived from the computed monthly $ETOP01 T_{as}$, as described earlier (see Fig. 3D, E). The frozen-ground type was diagnosed by Equations 3–7.

Results

The present-day permafrost distribution reconstructed from present-day observed freezing/thawing indices (Fig. 4A) was compared with the IPA map (Fig. 4) in the NE Asia sector. It showed a satisfactory correspondence of the at-large permafrost coverage with the map. In particular, areas of climate-driven permafrost (dark blue in Fig. 4A) are largely within those of continuous permafrost (darkest blue in Fig. 4B), and the boundaries of permafrost (bluish colours; the southern limit of ‘discontinuous permafrost’ as used in field research) in Fig. 4B generally coincide with those between environmentally conditional permafrost (EP; blue colour) and seasonally freezing (Sf; greenish colours) in Fig. 4A. However, regional and local discrepancies are still apparent in regions such as the southern part of Primorye region, Mount Daisetsu in Hokkaido, NW Mongolia and south of the Qinghai-Xizang (Tibet) Plateau, where the index-based method (Equations 3–7) fails to predict the presence of permafrost. Similarly, the extent of seasonally frozen ground from the revised formula shows overall agreement with previous studies (Zhang *et al.* 2003). The exception is the middle China Plain between 28 and 34°N where the formula failed to predict ‘intermittent freezing’ regions (Im). Since the limits of the Im regions are determined by a freezing index value of zero, this probably implies the limitations of using the freezing index based on a monthly mean that cannot capture intra-month variations.

Figure 5 shows the frozen-ground distribution map reconstructed from the PMIP2 simulation ensemble for the pre-industrial conditions (0 ka; Fig. 5A) and LPM (21 ka; Fig. 5B). The mode distribution at 0 ka shows results largely consistent with the IPA map (Fig. 4B), seasonally freezing ground (Zhang *et al.* 2003: fig. 1) and the map reconstructed from freezing/thawing indices calculated from observed temperature (Fig. 4A). The southern limit of overall permafrost areas (CP + EP; bluish coloured; Fig. 5A) north of 45°N corresponds well to the limit of latitudinal (i.e. climate-induced) permafrost in the IPA map in Fig. 4B. This gives confidence to the following map that reconstructs permafrost conditions at the time of the LPM.

The map showing permafrost in NE Asia at the time of the LPM (Fig. 5B) shows the wide expanse of both perennially and seasonally frozen ground in the area between 25 and 60°N. The regional nature of this distribution is examined below. For comparison with observation-based extents, see also Vandenberghe *et al.* (2014).

The central Siberia highlands and Altai to the south (–45–60°N, 90–100°E) were largely underlain by permafrost, extending south to central Asia at around 45°N. This is consistent with previous observation-based studies that identified the presence of permafrost from evidence such as polygonal structures, as well as possible deep seasonal freezing in central Asia (Baulin & Danilova 1984; Baulin *et al.* 1992).

In Mongolia, the western and central highlands and eastern (including Inner) Mongolia (–45–50°N, 100–115°E) were largely underlain by permafrost. The Daxinganlin and Xiaoxinganlin Mountain regions were extensively underlain by continuous permafrost in mountainous areas (alpine permafrost) and by discontinuous permafrost in the foothills. Velichko & Nechaev (1992) noted that ‘permafrost was distributed (at least, sporadically) up to 45°30’N’, citing Gravis & Lisun (1974).

Large areas around the northern coast of the Sea of Japan (–40–55°N, 130–145°E) were largely underlain by permafrost at the LPM, including continuous permafrost within the coastal Primorye regions (Baulin & Danilova 1984; Ono 1990; Baulin *et al.* 1992; Velichko & Nechaev 1992). Ono (1990, 1991) drew the southern boundary of continuous permafrost between Sakhalin and Hokkaido, and the southern boundary of discontinuous permafrost south of Hokkaido. Correspondingly, Sakhalin was mostly occupied by permafrost, with continuous permafrost on the mountain ridges, and in Japan’s northern Hokkaido by patches of permafrost and seasonal frost. On the continental side, Xu *et al.* (1988) suggested the southern boundary of permafrost was at 42°N, in the eastern sector of east China (around 120–130°E). Although Xu *et al.* (1988) did not clearly mention the nature of the permafrost zones, we speculate from their discussion that they implied sporadic permafrost. Permafrost was present in most of the high-altitude areas stretching down to about 42°N along the coast from the Sikhote-Alin Mountains, with less extensive coverage along the mountain ranges between China and the Korean Peninsula, including Changbaishan (Pjaktusan) Mountain. The northeastern China Plain was underlain by permafrost to the north from about 43°N, and to the south by seasonally frozen ground (Jin *et al.* 2007).

The nature of the ground thermal regime at the LPM from central Asia to central China – spreading from the Gobi desert, through the Ordos Plateau, to the lowlands of what are now the Bohai and Yellow Seas – is not clearly known. Baulin *et al.* (1992) categorized this region as deep, seasonal frost, whereas French (2007) classified the western part of this region as discontinuous permafrost. Vandenberghe *et al.* (2004, 2012) drew the southern limit of continuous permafrost at 38°N. Ono (1990) supposed the southern limit of the (sporadic, alpine) permafrost zone in this region was at around 37°N (located at Wutaishan Mountain, on the

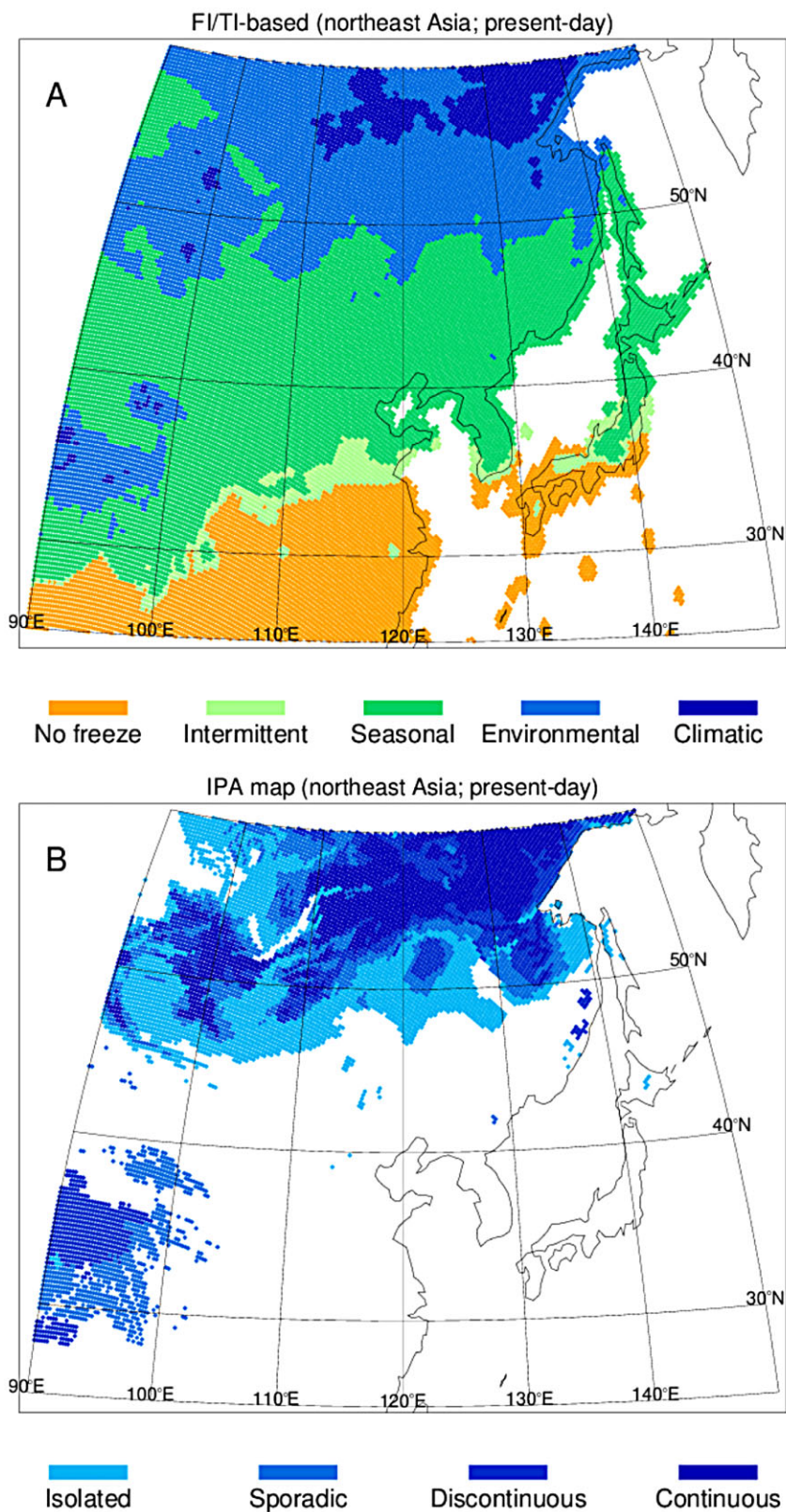


Fig. 4. A. Northeast Asia frozen ground distribution produced from the observed freezing/thawing indices. The categories are climate-driven permafrost (CP; dark blue), environmentally conditional permafrost (EP; blue), seasonal freezing (Sf; green), intermittent freezing (Im; pale green) and no freezing (Nf; orange). B. Permafrost distribution from the IPA map for the same section. Continuous, discontinuous, sporadic and isolated permafrost are shown by the gradation of blue colours (from dark to pale). This figure is available in colour at <http://www.boreas.dk>

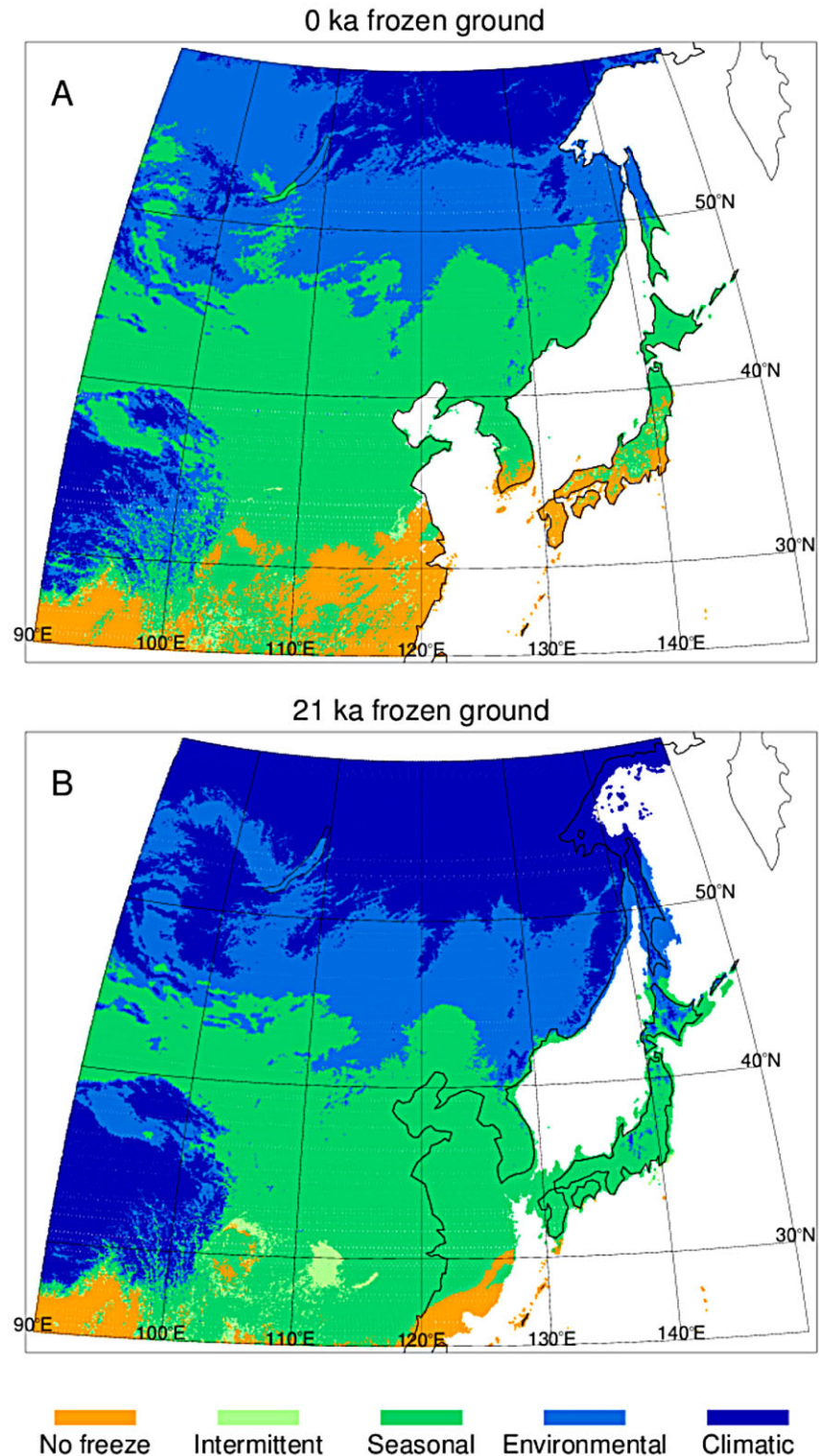


Fig. 5. Northeast Asia frozen-ground distribution reconstructed from the PMIP2 simulations for the period of (A) pre-industrial (0 ka) and (B) LPM (21 ka). The frozen-ground type was determined by the ensemble mode (i.e. most frequent value) at each ETOPO1 grid location. When a tie at the highest frequency occurred, the type closer to permafrost (or the colder condition) was chosen. This figure is available in colour at <http://www.boreas.dk>

opposite side of the Yellow River), following Xu *et al.* (1988). In our reconstructed map, this area is almost entirely underlain by long-lasting seasonal freezing (Sf), with only sporadic patches of permafrost of alpine characteristics in areas south of 40°N that connect to

the Wutai Mountains. Intermittent freezing was rare, except at the rim of the Sichuan basin and in the lowland area near Dongting Lake. The southern limit of freezing was at 28–30°N in the coastal lowlands, 25°N in interior central China and to the south of the

Table 2. Advancement of LPM (21 ka) southern limit of frozen ground relative to the present-day (0 ka) for 10°E strips from 90 to 140°E for climate-driven permafrost zones (CP), environmentally conditional permafrost zone (EP) and any freezing zones. The southern limit of the zones is shown for respective periods in the upper two rows, while the southward advancement (Δ) from LPM to the present-day is shown by latitudinal degree and actual distance in the third row.

| Strip | CP | | EP | Freezing | | |
|---------|----------|--------|-------|----------|-------|------|
| | °N | km | °N | km | °N | |
| 90–100 | 0 ka | >60.00 | 46.00 | | 30.00 | |
| | 21 ka | 46.75 | 45.00 | | 29.50 | |
| | Δ | >13.25 | >1474 | 1.00 | 111 | 0.50 |
| 100–110 | 0 ka | 59.75 | 46.25 | | 32.75 | |
| | 21 ka | 50.75 | 45.25 | | 32.00 | |
| | Δ | 9.00 | 1001 | 1.00 | 111 | 0.75 |
| 110–120 | 0 ka | 54.50 | 45.75 | | 33.75 | |
| | 21 ka | 50.50 | 41.00 | | 26.75 | |
| | Δ | 4.00 | 445 | 4.75 | 528 | 7.00 |
| 120–130 | 0 ka | 55.50 | 47.75 | | 36.75 | |
| | 21 ka | 50.25 | 42.00 | | 30.50 | |
| | Δ | 5.25 | 584 | 5.75 | 640 | 6.25 |
| 130–140 | 0 ka | 55.00 | 48.25 | | 39.50 | |
| | 21 ka | 49.50 | 42.75 | | 33.25 | |
| | Δ | 5.50 | 612 | 5.50 | 612 | 6.25 |

Himalayan Range in the 90–100°E sector (see also Zhao *et al.* 2014). The entire area covering the Qinghai-Xizang (Tibet) Plateau and Qilian Shan was occupied by permafrost, largely continuous in the two mountainous areas. This is consistent with previous studies (e.g. Jin *et al.* 2007).

For the LPM period, it seems the southern limits of both permafrost and seasonal freezing shifted to the south due to a cooler environment. Table 2 summarizes the changes at the southern borders of both climate-driven and environmentally conditional permafrost and seasonally frozen ground areas. This border is determined as the southernmost latitude for each 10° longitudinal sector at which the percentage of an occupying frozen ground type (e.g. environmentally conditional permafrost) decreases to less than 50% (yielding, in this case, to seasonally freezing). The southward shift of climate-driven permafrost varied from 450 to 1500 km across the NE Asian region – greater in the western sector (90–110°E) than in the eastern sector (110–140°E). The aggradation of permafrost in central Siberia down to the south of the Altai contributed significantly to this regional difference. In contrast, southward shifts of the southern limit of overall permafrost and seasonally frozen ground areas increase in the reverse, from west to east, ranging from 110 to 650 km for overall permafrost, and from 60 to 780 km for seasonally frozen ground – an average of 400–460 km in east Asia.

Figure 6 shows diversity maps of categorized frozen-ground types, measured by the quantity H , known as the Shannon–Wiener index, and defined by the classi-

fication probability, p_i , for the i th category (Shannon 1948):

$$H = -\sum_i p_i \ln(p_i). \quad (9)$$

In general, areas of relatively high intermodel diversity are located around the borders between adjacent categories – such as CP and EP, or Sf (or Im) and Nf. The highest diversity (shown in reddish colours in Fig. 6) tends to show up consistently in the southern regions, especially at the borders between freezing and no freezing, in both the 0 ka and 21 ka results. A lack of intermittently frozen ground in these regions may be due in part to this high variability of simulated climate among the numerical models.

Discussion

Sensitivity to atmospheric lapse rate

In this study we assumed a constant atmospheric lapse rate. This value, kept common for the entire area and for all months, was 6.5°C km⁻¹ (NOAA 1976). It is generally understood to be close to the radiative–conductive equilibrium state of the current atmosphere (Hartmann 1994; Wallace & Hobbs 2006). In reality, the atmospheric lapse rate varies both in time and space, and its value depends on many factors. Moisture content of the ambient atmosphere is a primary factor; the drier the atmosphere, the greater the value approaches the dry adiabatic condition of 9.8°C km⁻¹. From this point of view, temperature extrapolation should focus upon the varying lapse rate reflecting the vertical profile of the atmosphere, including aridity/humidity, especially for application to the continental interior conditions. This may be accomplished by using tropospheric temperature, which would require additional data (variables) and computational effort, in contrast to our principle for simplicity. Thus, we examined the sensitivity of lapse-rate values toward the resulting frozen-ground categories and their distribution. Lapse rate was kept constant in every case, although the value was shifted from 4.5 to 8.5°C km⁻¹. A summary of the LPM results is tabulated in Table 3. This sensitivity test shows an almost linear response to the atmospheric lapse rate in all frozen ground categories. The zones of 2000 to 5000 m a.s.l. elevation were found to be most sensitive, although the total spatial contribution was, at most, 3.3 million km². The resulting frozen-ground distribution largely showed only slight differences.

Another limitation of the current method as regards the vertical atmospheric profile is its seasonality – especially the formation of an inversion layer. During winter, this layer typically forms in continental, high-latitude regions, keeping surface temperature very cold

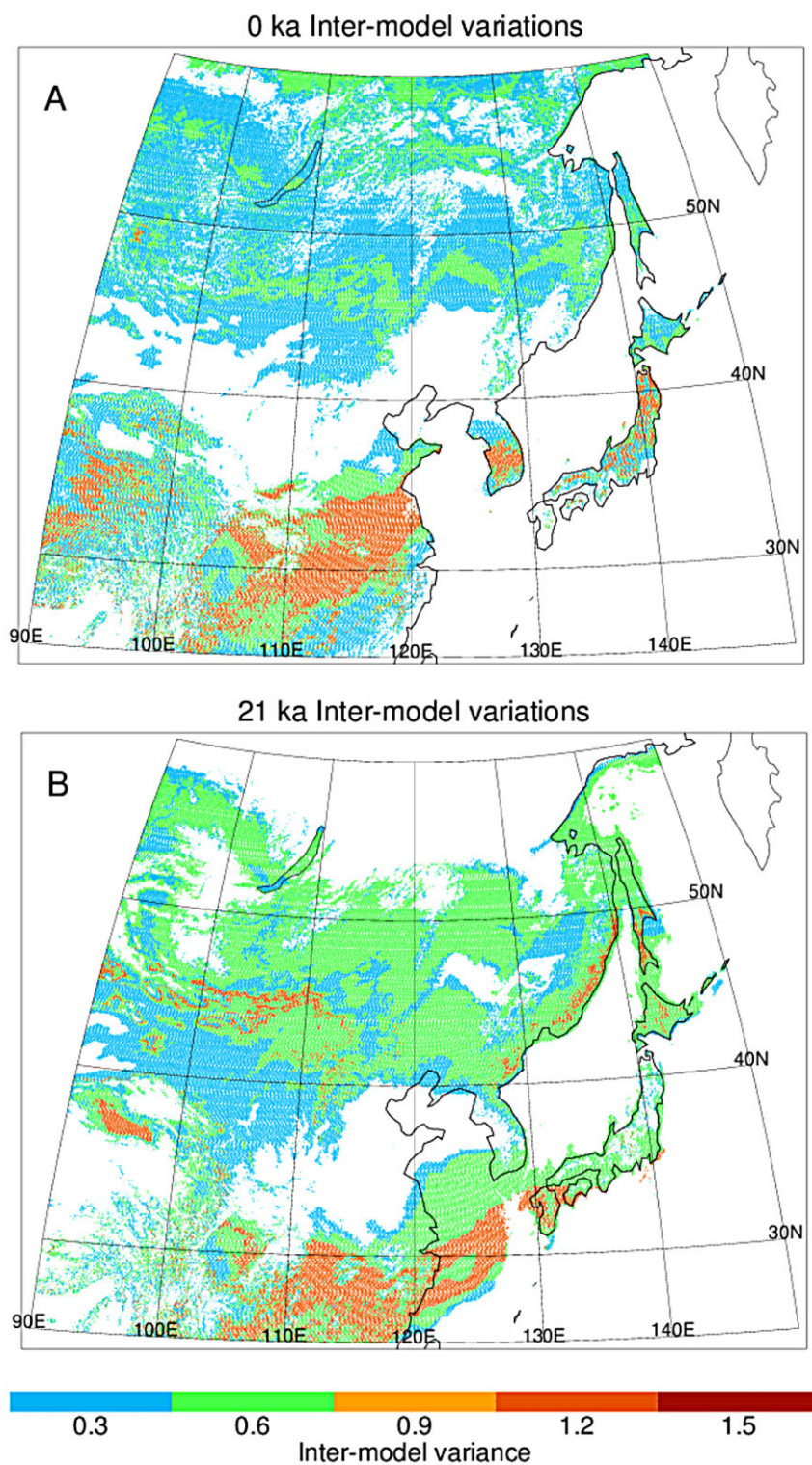


Fig. 6. The across-model diversity of reconstructed frozen-ground type for the period of (A) pre-industrial (0 ka) and (B) LPM (21 ka). This figure is available in colour at <http://www.boreas.dk>

and fostering the development or sustainment of frozen ground. The horizontal and vertical resolution of the PMIP2 simulations, however, did not produce this inverse layer appropriately (not shown).

Simulated climate and statistical downscaling

The horizontal resolution of the original PMIP2 simulations was, at its finest, 124 by 64 – about 2.8° east–

Table 3. Sensitivity of the LPM frozen-ground area to the atmospheric lapse rate. The examined range of the atmospheric lapse rate was 4.0–8.0°C km⁻¹. The unit of the numbers is in 10⁶ km² (°C km⁻¹)⁻¹. ‘–’ denotes no grids in the category.

| Altitude (m) | –1000 | –2000 | –3000 | –4000 | –5000 | –6000 | 6000– | Total |
|--------------|-------|-------|-------|-------|-------|-------|-------|-------|
| CP | –0.64 | 0.33 | 0.95 | 1.57 | 1.09 | 0.02 | 0.00 | 3.32 |
| EP | 0.56 | 0.10 | –0.00 | –0.65 | –0.77 | –0.01 | – | –0.77 |
| Sf | –1.27 | –0.15 | –0.50 | –0.46 | –0.08 | – | – | –2.45 |
| Im | –0.15 | 0.22 | –0.05 | – | – | – | – | 0.02 |

west and 2.8° north–south (Table 1). It is obvious that the downscaled maps of this study better captured the regional to local characteristics of the predicted frozen-ground distribution (Figs. 5, 6) when compared with the earlier coarser version by Saito *et al.* (2009; Figs. 3, 5). In constructing a downscaling method for frozen-ground distribution, temperature and topography are the necessary data. However, direct use of a bilinear interpolation of surface air temperature from a coarse grid system to a finer one would result in a loss of the advantage of local topographic information from the fine-scale digital relief model (cf. Levvasseur *et al.* 2011: figs 3a, 4a, 7a, 8a). An additional step in temperature extrapolation for mean sea level before applying the downscale regriding to the finer ETOPO1 grids is the key to maximizing the utilization of topographic information. This is also a cost-to-benefit matter; more elaborate and sophisticated statistical models can be constructed utilizing additional available information.

Multiple sources and a hierarchy of unknowns and uncertainties exist when constructing and applying a statistical classification. The first is calibration data. In this study, present-day permafrost distribution data were used. As stated in the ‘Methods’ section, not all of the grid data in the IPA map are based on geomorphological or borehole evidence, but rather interpolated cartographically using temperature, elevation and other information. Even when local evidence is present for an area, it is not trivial to determine the relative areal coverage of permafrost in the area (i.e. is it continuous permafrost underlying more than 90% of the area or discontinuous permafrost occupying a lesser percentage, etc.). Updates of permafrost distribution maps, such as those by Jorgenson *et al.* (2008) for Alaska, are important for improving performance.

The second issue is the gap between equilibrium and transitional permafrost states. On the one hand, calibration data (e.g. the IPA map and other present-day evidence) reflect the current ground thermal regime; this is not necessarily in equilibrium with recent climate (Shur & Jorgenson 2007; Romanovsky *et al.* 2010). On the other hand, the 21 ka PMIP2 products are, rather, a time-slice simulation, implicitly assuming equilibrium conditions at the time period examined. There is a gap, therefore, in the construction (present-day data) and application (LPM simulations) of the method.

Uncertainties are also present in the simulated climate. The common deficiencies of the PMIP2 simulated climate – for example, the warm biases in the western part of mid-latitude Eurasia that hindered development of permafrost in the area – have been recognized (e.g. Saito *et al.* 2009; Levvasseur *et al.* 2011). But it has not been extensively investigated as to how well the PMIP2 simulations reproduced the LPM NE Asia climate. We have recognized substantial variation among the models – for example, in the 30–60°N, 80–100°E sector, from the Tibetan Plateau to the Altai to central Siberia (see the contrast between Figs. 7 and 8 of Levvasseur *et al.* 2011). It would be unwise, therefore, to reconstruct a satisfactory map from simulations prone to uncertainties and biases. Updated datasets are now in production from more realistic and finer-scale products of the PMIP3 climate simulations conducted by the newer, state-of-the-art GCMs and ESMs (Saito *et al.* 2013b).

Latitude–altitude relationship

The latitudinal variation of the lower limit of permafrost (H_P) serves as one of the key comparison targets for examining the validity and appropriateness of our study. For example, Figs 7 and 8 show the latitude–altitude cross-section at different 10° longitudinal sectors for the present-day (for the selected longitudinal sectors from the simulated maps – 7A and 7B, and the IPA map – 7C and 7D) and for LPM, respectively. In the 90–100°E sector, lines separating the adjacent frozen ground type are almost parallel to each other, implying a zonally aligned, meridionally smooth distribution of mean-sea-level air temperature. The gradient of the lower limit (H_P) of simulated 0 ka climate-driven permafrost was –104 m per 1° along the line *a* (30–40°N) and –174 m per 1° along the line *b* (43–59°N), resulting from a gentle gradient of the background temperature in the former latitudes, and a steep gradient in the latter (cf. Fig. 3A, C). The average latitudinal variation of the observed lower limit of permafrost (the $H_P=9400-160 L_N$, where L_N is the latitude in degrees north, shown by dashed line; taken from Matsuoka 2003) is in strong agreement with the lower limit of environmentally conditional permafrost in this sector. Other H_P observations found in the literature (shown by numbers in the plots) are also plotted. Definition of these values, however, is either not clear or is shared

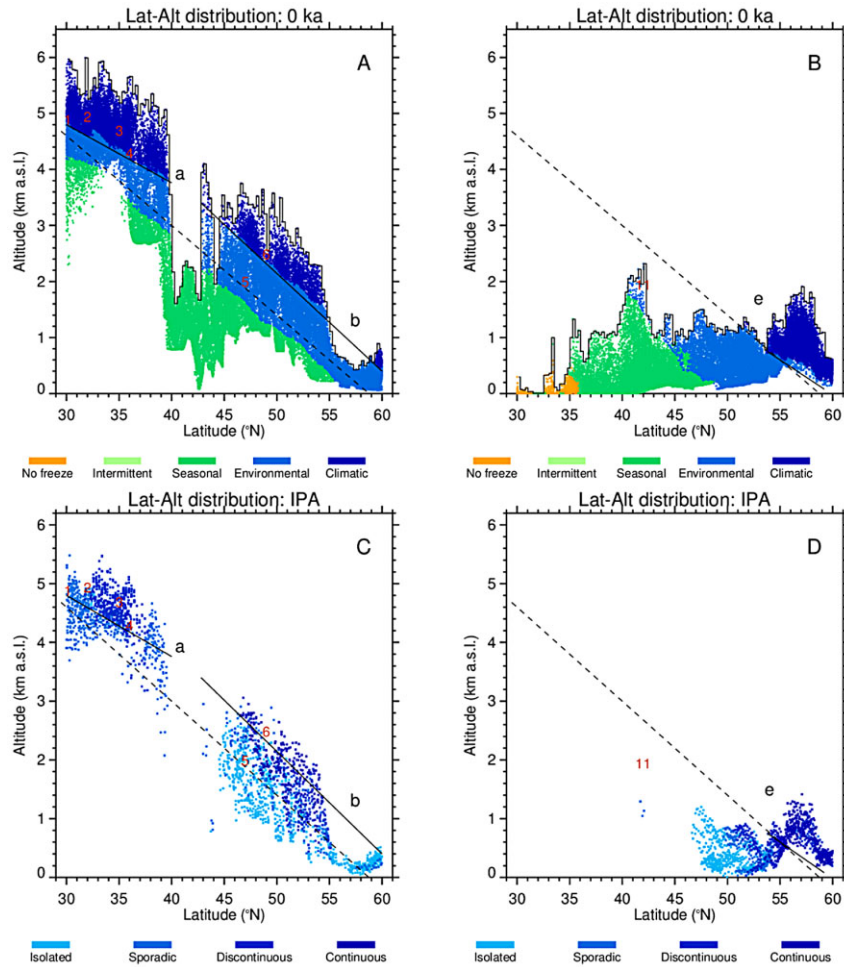


Fig. 7. Latitude–altitude cross-section of the present-day frozen-ground distribution reconstructed from the PMIP2 simulations in 90–150°E, shown for 10° longitude strips for (A) 90–100°E and (B) 120–130°E. C, D. Same as A, B, respectively, except that the data are taken from the IPA map. Numbers in red denote the position of the lower limit of permafrost found in the literature (Matsuoka 2003). 1 = Nyainqentanglha; 2 = Queer; 3 = West Kunlun; 4 = East Kunlun; 5 = Hangai; 6 = north Altai; 11 = Chanbai. Lines a, b and e show the average latitudinal slope of the lower limit of permafrost in the respective areas. Dashed line is the observed lower limit of permafrost (Matsuoka 2003). This figure is available in colour at <http://www.boreas.dk>

between the studies. Reflecting this variability, these values correspond to different type of permafrost in the IPA map (Fig. 7C, D). Similarly, they coincide with the lower limit of either climate-driven permafrost (1, 2, 3, 4, 6, 8 and 11 for 0 ka, and 13, 14 and 19 for 21 ka) or environmentally conditional permafrost (5, 7, 9, 10 and 12 for 0 ka, and 15, 16, 17 and 18 for 21 ka). In either case, matching of these observational indicators illustrates a reasonably successful reconstruction of frozen-ground distributions.

Matsuoka (2003) has shown that the latitudinal lapse rate remains similar from arid continental regions to humid or coastal regions, although H_P *per se* descends toward the coast by about 1000 m. Figure 7A (90–100°E) and 7B (120–130°E) have successfully reproduced this feature, which can also be verified by similar cross-sections produced from the IPA map (Fig. 7C, D), particularly between 33 and 43°N. In the higher latitudes (e.g. eastern Mongolia, the Daxinganlin Mountains, the northeast China Plain) and coastal regions (the Sikhote-Alin Mountains), however, local variations and undulations appear to be more effective.

Similar plots for LPM reconstruction are shown in Fig. 8, which displays the overall descent of the H_P line throughout the entire region because of cooler temperatures, with the latitudinal lapse rate unchanged. For example, compare lines *a* and *b* in Fig. 7A (90–100°E) with line *f* (100 m per 1°) and line *g* (191 m per 1°), respectively, in Fig. 8A; and line *e* in Fig. 7B (120–130°E) with line *j* (142 m per 1°) in Fig. 8D. The descent of the reconstructed H_P was about 400–800 m in NE Asia – smaller than the values shown in previous studies, such as 1200–1500 m (Xu *et al.* 1988) or 1500 m (Ono 1990, 1991). The source of this discrepancy is not clear, but may result in part from the factors discussed above. This also implies possible additional effects from neglected factors such as water abundance, snow cover, vegetation, soil characteristics and local and micro-topography.

Conclusion

A statistical approach to estimating large-scale frozen-ground distribution from surface air temperature

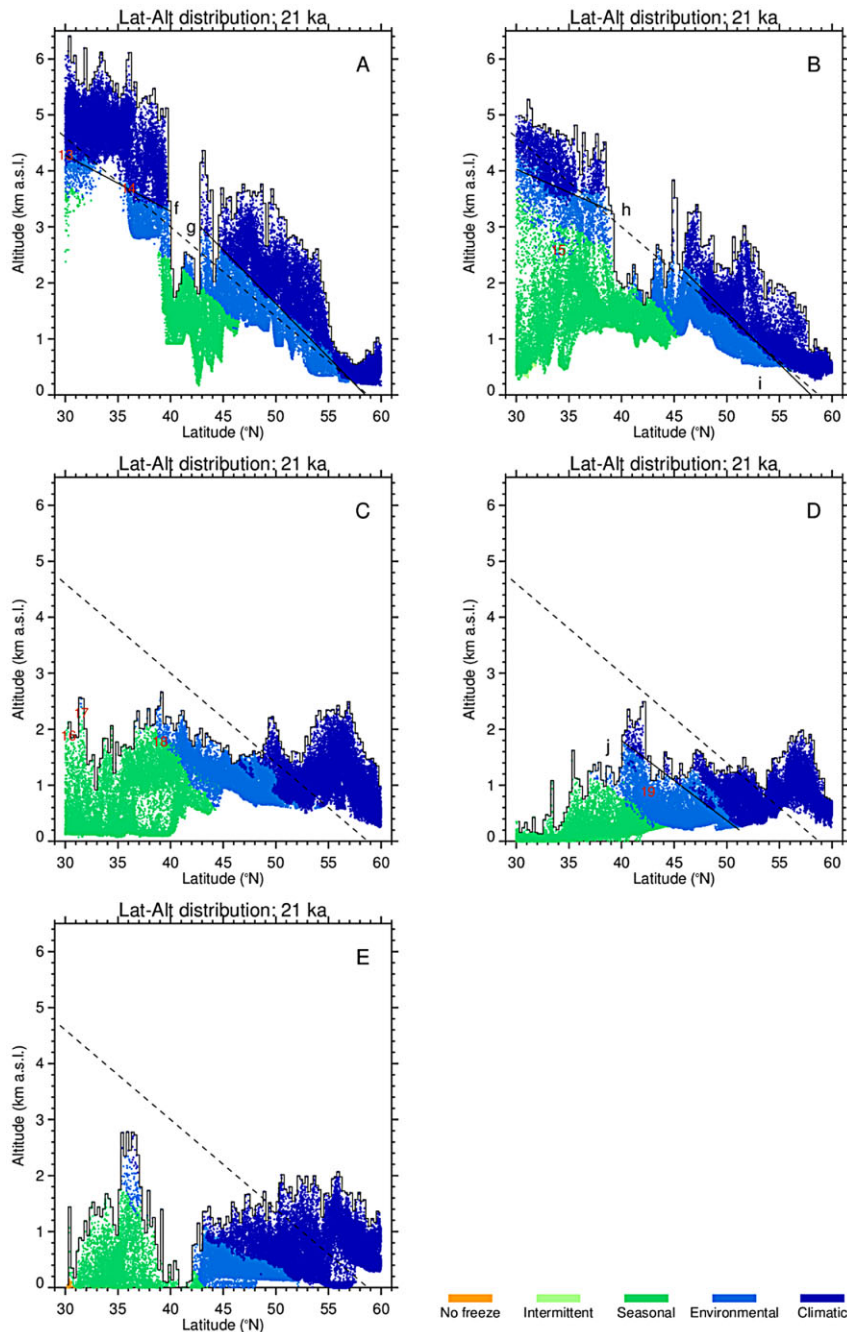


Fig. 8. Latitude–altitude cross-section of the LPM frozen-ground distribution reconstructed from the PMIP2 simulations for (A) 90–100°E, (B) 100–110°E, (C) 110–120°E, (D) 120–130°E and (E) 130–140°E. Numbers in red denote the position of the lower limit of permafrost found in literature. 13 = south in Qinghai-Xizang (Tibet) Highway; 14 = Naj Tal (13–14: Cheng 1983); 15 = Taibai; 16 = Tianmu; 17 = Wushan; 18 = Wutaishan; 19 = Chanbai (15–19: Xu *et al.* 1988). Lines f, g, h, i and j show the average latitudinal slope of the lower limit of permafrost in the respective areas. Dashed line is the observed lower limit of permafrost (Matsuoka 2003). This figure is available in colour at <http://www.boreas.dk>

(namely, freezing and thawing indices) has been extended to the production of a high-resolution (1 arc-minute, approximately 2 km in latitude) map using downscaling techniques. This methodology was applied to PMIP2 GCM simulation outputs for two periods – the pre-industrial period (approximately equivalent to the present day) and the Last Glacial Maximum (to approximate the Last Permafrost Maximum (LPM) distribution). Results were compared with evidence-based literature and maps and show overall correspondence and consistency with

previous studies. The southern extent of permafrost at the time of the LPM was greater in the western sector (central Asia to central Siberia, ~1500 km) for climate-driven permafrost, while it was greater in the central to coastal sectors for environmentally conditional permafrost and seasonally frozen ground (up to 700 km). Similarly, the lower limit of alpine permafrost descended by between 500 and 1000 m.

The advantage of the statistical method lies in simplicity in construction and flexibility in application. Because only surface air temperature and topographic

data were used to estimate frozen-ground distribution, it is evident that the reconstructed maps are oversimplified due, in part, to neglect of other important local factors. Therefore, this study should be regarded as a first-order estimate that may need to be refined through the use of more physically based approaches. Numerical modelling of subsurface dynamics of energy, water and materials, in combination with large-scale eco-climate models, is clearly required. It is also necessary to collect further field data and increase understanding of the physical, chemical and ecological aspects of permafrost evolution in the past.

Acknowledgements. – This study was partially supported by the U.S. National Science Foundation under ARC-1107524. The authors are indebted to the two anonymous reviewers for their constructive comments and instrumental suggestions to improve the original manuscript. The authors thank Nate Bauer (International Arctic Research Center, University of Alaska Fairbanks) for language proofreading and editing of the manuscript. Further editing and language upgrading was undertaken by the co-editors, Professor Jef Vandenberghé and Professor Hugh French.

References

- Alexeev, V. A., Nicolsky, D. J., Romanovsky, V. E. & Lawrence, D. M. 2007: An evaluation of deep soil configurations in the CLM3 for improved representation of permafrost. *Geophysical Research Letters* 34, L09502, 663, doi: 10.1029/2007GL029536.
- Amante, C. & Eakins, B. W. 2009: ETOPO1 1 arc-minute global relief model: procedures, data sources and analysis. *NOAA Technical Memorandum NESDIS NGDC-24*, 19 pp.
- Anisimov, O. A. & Nelson, F. E. 1997: Permafrost zonation and climate change in the Northern Hemisphere: results from transient general circulation models. *Climatic Change* 35, 241–258.
- Baulin, V. V. & Danilova, N. S. 1984: Dynamics of Late Quaternary permafrost in Siberia. In Velichko, A. A. (ed.): *Late Quaternary Environments of the Soviet Union*, 69–78. University of Minnesota Press, Minneapolis.
- Baulin, V. V., Danilova, N. S., Nechayev, V. P., Péwé, T. L. & Velichko, A. A. 1992: Permafrost: maximum cooling of the Last Glaciation (about 20,000 to 18,000 yr B.P.). In Frenzel, B., Pécsi, M. & Velichko, A. A. (eds.): *Atlas of Paleoclimates and Paleoenvironments of the Northern Hemisphere*, p. 49. Gustav Fischer Verlag, Stuttgart.
- Boeckli, L., Brenning, A., Gruber, S. & Noetzi, J. 2012: A statistical approach to modelling permafrost distribution in the European Alps or similar mountain ranges. *The Cryosphere* 6, 125–140.
- Braconnot, P., Otto-Bliessner, B., Harrison, S., Joussaume, S., Peterchmitt, J.-Y., Abe-Ouchi, A., Crucifix, M., Driesschaert, E., Fichet, T., Hewitt, C. D., Kageyama, M., Kitoh, A., Laine, A., Loutre, M.-F., Marti, O., Merkel, U., Ramstein, G., Valdes, P., Weber, S. L., Yu, Y. & Zhao, Y. 2007: Results of PMIP2 coupled simulations of the Mid-Holocene and Last Glacial Maximum – part 1: experiments and large-scale features. *Climate of the Past* 3, 261–277.
- Brown, J., Ferrians, Jr., O. J., Heginbottom, J. A. & Melnikov, E. S. 1997: *Circum-Arctic Map of Permafrost and Ground-Ice Conditions*, Geological Survey for the International Permafrost Association. USGS Circum-Pacific Map Series, Map CP-45, scale: 1:10,000,000. Washington, DC.
- Burn, C. R. & Nelson, F. E. 2006: Comment on ‘A projection of severe near-surface permafrost degradation during the 21st century’ by David M. Lawrence and Andrew G. Slater. *Geophysical Research Letters* 33, L21503. doi: 10.1029/2006GL027077.
- Cheng, G. 1983: Vertical and horizontal zonation of high-altitude permafrost. In Rooney, R. C. (ed.): *Proceedings of the Fourth International Conference on Permafrost*, 139–144. National Academy Press, Washington, DC.
- Clark, P. U. & Mix, A. C. 2002: Ice sheets and sea level of the Last Glacial Maximum. *Quaternary Science Reviews* 21, 1–7.
- Collins, W., Bitz, C., Blackmon, M., Bonan, G., Bretherton, C., Carton, J., Chang, P., Doney, S., Hack, J., Henderson, T., Kiehl, J., Large, W., McKenna, D., Santer, B. & Smith, R. 2001: The Community Climate System Model: CCSM3. *Bulletin of the American Meteorological Society* 82, 2357–2376.
- Delisle, G. 1998: Numerical simulation of permafrost growth and decay. *Journal of Quaternary Science* 13, 325–333.
- Farr, T. G., Rosen, P. A., Caro, E., Crippen, R., Duren, R., Hensley, S., Kobrick, M., Paller, M., Rodriguez, E., Roth, L., Seal, D., Shaffer, S., Shimada, J., Umland, J., Werner, M., Oskin, M., Burbank, D. & Alsdorf, D. 2007: The Shuttle Radar Topography Mission. *Review of Geophysics* 45, RG2004, doi: 10.1029/2005RG000183.
- Frauenfeld, O. W., Zhang, T. & McCreight, J. L. 2007: Northern hemisphere freezing/thawing index variations over the twentieth century. *International Journal of Climatology* 27, 47–63.
- French, H. M. 2007: *The Periglacial Environment*. 458 pp. Wiley, Chichester.
- Gordon, C., Cooper, C., Senior, C., Banks, H., Gregory, J., Johns, T., Mitchell, J. & Wood, R. 2000: The simulation of SST, sea ice extents and ocean heat transports in a version of the Hadley Centre coupled model without flux adjustments. *Climate Dynamics* 16, 147–168.
- Gravis, G. F. & Lisun, A. M. 1974: Rhythmic stratigraphy of Quaternary deposits in Mongolia based on palynology and history of the permafrost development. In Melnikov, P. I. (ed.): *Geokriologicheskie usloviya Mongolskoj Narodnoj Respubliki*, 148–186. Nauka, Moscow (in Russian).
- Gruber, S. 2012: Derivation and analysis of a high-resolution estimate of global permafrost zonation. *The Cryosphere* 6, 221–233.
- Harris, S. A. 1981: Climatic relationships of permafrost zones in areas of low winter snow-cover. *Arctic* 34, 64–70.
- Harris, S. A. 1982: Identification of permafrost zones using selected permafrost landforms. *Climate and Permafrost, 4th Canadian Permafrost Conference*, 49–58.
- Hartmann, D. L. 1994: *Global Physical Climatology*. 408 pp. Academic Press, San Diego.
- Hasumi, H. & Emori, S. 2004: *K-1 coupled GCM (MIROC) description, Technical Report 1*, 34 pp. Center for Climate System Research, Univ. of Tokyo, Kashiwa.
- Hubberten, H. W., Andreev, A., Astakhov, V. I., Demidov, I., Dowdeswell, J. A., Henriksen, M., Hjort, C., Houmark-Nielsen, M., Jakobsson, M., Kuzmina, S., Larsen, E., Pekka Lunkka, J., Lyså, A., Mangerud, J., Möller, P., Saarnisto, M., Schirmermeister, L., Sher, A. V., Siegert, C., Sieger, M. J. & Svendsen, J. I. 2004: The periglacial climate and environment in northern Eurasia during the Last Glaciation. *Quaternary Science Reviews* 23, 1333–1357.
- Jin, H., Li, S., Cheng, G., Wang, S. & Li, X. 2000: Permafrost and climatic change in China. *Global and Planetary Change* 26, 387–404.
- Jin, H. J., Chang, X. L. & Wang, S. L. 2007: Evolution of permafrost on the Qinghai-Xizang (Tibet) Plateau since the end of the late Pleistocene. *Journal of Geophysical Research* 112, F02S09, doi: 10.1029/2006JF000521.
- Jorgenson, T., Yoshikawa, K., Kanevskiy, M., Shur, Y., Romanovsky, V., Marchenko, S., Grosse, G., Brown, J. & Jones, B. 2008: *Permafrost Characteristics of Alaska*. The Permafrost Laboratory, Geophysical Institute, University of Alaska, Fairbanks. Available at: http://permafrost.gi.alaska.edu/sites/default/files/AlaskaPermafrostMap_Front_Dec2008_Jorgenson_etal_2008.pdf and http://permafrost.gi.alaska.edu/sites/default/files/AlaskaPermafrostMap_Back_Jun2008_Jorgenson_etal_2008.pdf (accessed 6 August 2013).
- Kitover, D. C., Renssen, H., Van Balen, R. T. & Vandenberghé, J. 2012: Modeling permafrost response of the last glacial termination: first results of the VAMPER model. In Hinkel, K. M. (ed.): *Proceedings of the Tenth International Conference on Permafrost* 1, 209–214. The Northern Publisher, Salekhard.

- Lawrence, D. M. & Slater, A. G. 2005: A projection of severe near-surface permafrost degradation during the 21st century. *Geophysical Research Letters* 32, L24401, doi: 10.1029/2005GL025080.
- Lawrence, D. M. & Slater, A. G. 2006: Reply to comment by C. R. Burn and F. E. Nelson on 'A projection of near-surface permafrost degradation during the 21st century'. *Geophysical Research Letters* 33, L21504, doi: 10.1029/2006GL027955.
- Lawrence, D. M. & Slater, A. G. 2010: The contribution of snow condition trends to future ground climate. *Climate Dynamics* 34, 969–981.
- Levassasseur, G., Vrac, M., Roche, D. M., Paillard, D., Martin, A. & Vandenberghé, J. 2011: Present and LGM permafrost from climate simulations: contribution of statistical downscaling. *Climate of the Past* 7, 1225–1246.
- Marti, O., Braconnot, P., Bellier, J., Benschila, R., Bony, S., Brockmann, P., Cadulle, P., Caubel, A., Denvil, S., Dufresne, J.-L., Fairhead, L., Filiberti, M.-A., Fichet, T., Friedlingstein, P., Grandpeix, J.-Y., Hourdin, F., Krinner, G., Lévy, C., Musat, I. & Talandier, C. 2005: The new IPSL climate system model: IPSLCM4. *Note du Pôle de Modélisation* 26, 1–86.
- Matsuoka, N. 2003: Contemporary permafrost and periglacialization in Asian high mountains: an overview. *Zeitschrift für Geomorphologie, Supplementbände* 130, 145–166.
- Matsuoka, N. 2011: Climate and material controls on periglacial soil processes: toward improving periglacial climate indicators. *Quaternary Research* 75, 356–365.
- Milne, G. A. & Mitrovica, J. X. 2008: Searching for eustasy in deglacial sea-level histories. *Quaternary Science Reviews* 27, 2292–2302.
- National Oceanic and Atmospheric Administration (NOAA) 1976: *U.S. Standard Atmosphere, 1976. Technical Report 7709*. NOAA, Rockville, Maryland.
- Nelson, F. E. & Outcalt, S. I. 1987: Computational method for prediction and regionalization of permafrost. *Arctic and Alpine Research* 19, 279–288.
- Nelson, F. E., Anisimov, O. A. & Shiklomanov, N. I. 2002: Climate change and hazard zonation in the circum-arctic permafrost regions. *Natural Hazards* 26, 203–225.
- Nicolsky, D. J., Romanovsky, V. E., Alexeev, V. A. & Lawrence, D. M. 2007: Improved modeling of permafrost dynamics in a GCM land-surface scheme. *Geophysical Research Letters* 34, L08501, doi: 10.1029/2007GL029525.
- Ono, Y. 1990: The Northern Landbridge of Japan. *The Quaternary Research (Daiyonki kenkyuu)* 29, 183–192 (in Japanese).
- Ono, Y. 1991: Glacial and periglacial paleoenvironments in the Japanese Islands. *The Quaternary Research (Daiyonki kenkyuu)* 30, 203–211.
- Phipps, S. J. 2006: *The CSIRO Mk3L Climate System Model. Technical Report 3, Antarctic Climate & Ecosystems CRC*. Hobart, Tasmania.
- Renssen, H. & Vandenberghé, J. 2003: Investigation of the relationship between permafrost distribution in NW Europe and extensive winter sea-ice cover in the North Atlantic Ocean during the cold phases of the Last Glaciation. *Quaternary Science Reviews* 22, 209–223.
- Riseborough, D., Shiklomanov, N., Etzelmüller, B., Gruber, S. & Marchenko, S. 2008: Recent advances in permafrost modelling. *Permafrost and Periglacial Processes* 19, 137–156.
- Roche, D. M., Dokken, T. M., Goosse, H., Renssen, H. & Weber, S. L. 2007: Climate of the Last Glacial Maximum: sensitivity studies and model-data comparison with the LOVECLIM coupled model. *Climate of the Past* 3, 205–224.
- Roeckner, E., Bäuml, G., Bonaventura, L., Brokopf, R., Esch, M., Giorgetta, M., Hagemann, S., Kirchner, I., Kornbluh, L., Manzini, E., Rhodin, A., Schlese, U., Schulzweida, U. & Tompkins, A. 2003: *The atmospheric general circulation model ECHAM5. Part 1: model description. Technical Report 349*, Max-Planck Institute for Meteorology, Hamburg, 127 pp.
- Romanovsky, V. E., Smith, S. L. & Christiansen, H. H. 2010: Permafrost Thermal State in the Polar Northern Hemisphere during the International Polar Year 2007–2009: a Synthesis. *Permafrost and Periglacial Processes* 21, 106–116.
- Rozenbaum, G. E. & Shpolyanskaya, N. A. 1998: Late cenozoic permafrost history of the Russian Arctic. *Permafrost and Periglacial Processes* 9, 247–273.
- Saito, K. 2008: Arctic land hydro-thermal sensitivity under warming: idealized off-line evaluation of physical terrestrial scheme in global climate model. *Journal of Geophysical Research-Atmosphere* 113, D21106, doi: 10.1029/2008JD009880.
- Saito, K., Kimoto, M., Zhang, T., Takata, K. & Emori, S. 2007: Evaluating a high-resolution climate model: simulated hydrothermal regimes in frozen ground regions and their change under the global warming scenario. *Journal of Geophysical Research – Earth Surface* 112, F02S11, doi: 10.1029/2006JF000577.
- Saito, K., Marchenko, S., Romanovsky, V., Bigelow, N., Yoshikawa, K. & Walsh, J. 2009: Thermally-conditioned paleo-permafrost variations from global climate modeling. *Science Online Letters on the Atmosphere* 5, 101–104.
- Saito, K., Sueyoshi, T., Marchenko, S., Romanovsky, V., Otto-Bliesner, B., Walsh, J., Bigelow, N., Hendricks, A. & Yoshikawa, K. 2013b: LGM permafrost distribution: how well can the latest PMIP multi-model ensembles reconstruct? *Climate of the Past Discussion* 9, 1565–1597.
- Saito, K., Zhang, T., Yang, D., Marchenko, S., Barry, R. G., Romanovsky, V. & Hinzman, L. 2013a: Influence of the physical terrestrial arctic in the eco-climate system. *Ecological Applications*, doi: 10.1890/11-1062.1.
- Salas-Méila, D., Chauvin, F., Déqué, M., Douville, H., Guérémy, J., Marquet, P., Planton, S., Royer, J. & Tyteca, S. 2005: Description and validation of the CNRM-CM3 global coupled model. *CNRM Working Note* 103, 36 pp.
- Shannon, C. E. 1948: A mathematical theory of communication. *The Bell System Technical Journal* 27, 379–423 and 623–656.
- Shur, Y. L. & Jorgenson, M. T. 2007: Patterns of permafrost formation and degradation in relation to climate and ecosystems. *Permafrost and Periglacial Processes* 18, 7–19.
- Sueyoshi, T. & Hamano, Y. 2003: An attempt to obtain paleoclimatic information from the present permafrost distribution in Siberia. In Phillips, M., Springman, S. M. & Arenson, L. U. (eds.): *Proceedings of the Eighth International Conference on Permafrost*, 157–158. A. A. Balkema, Brookfield.
- United States Geological Survey (USGS) 2002: *GTOPO30 – Global 30 arc second elevation data*. U.S. Geological Survey, National Mapping Division, EROS Data Center.
- Vandenberghé, J., French, H. M., Gorbunov, A., Marchenko, S., Velichko, A. A., Jin, H., Cui, Z., Zhang, T. and Wan, X. 2014: The Last Permafrost Maximum (LPM) map of the Northern Hemisphere: permafrost extent and mean annual air temperatures, 25–17 ka BP. *Boreas* 43, 652–666.
- Vandenberghé, J., Cui, Z., Zhao, L. & Zhang, W. 2004: Thermal-contraction-crack Networks as Evidence for Late-Pleistocene Permafrost in Inner Mongolia, China. *Permafrost and Periglacial Processes* 15, 21–29.
- Vandenberghé, J., Renssen, H., Roche, D. M., Goosse, H., Velichko, A. A., Gorbunov, A. & Levassasseur, G. 2012: Eurasian permafrost instability constrained by reduced sea-ice cover. *Quaternary Science Reviews* 34, 16–23.
- Velichko, A. A. & Nechaev, V. P. 1992: Cryogenic regions during the Last Glacial Maximum (permafrost). In Frenzel, B., Pécsi, M. & Velichko, A. A. (eds.): *Atlas of Paleoclimates and Paleoenvironments of the Northern Hemisphere*, 108–109. Gustav Fischer Verlag, Stuttgart.
- Wallace, J. M. & Hobbs, P. V. 2006: *Atmospheric Science: An Introductory Survey*. 483 pp. Academic Press, San Diego.
- Washburn, A. L. 1980: Permafrost features as evidence of climatic change. *Earth-Science Reviews* 15, 327–402.
- Xu, S., Xu, D. & Pan, B. 1988: Outer limit of permafrost during the Last Glaciation in East China. In Senneset, K. (ed.): *Proceedings of the Fifth International Conference on Permafrost* 1, 268–273. Tapir Publishers, Trondheim.
- Yukimoto, S. & Noda, A. 2002: *Improvements of the Meteorological Research Institute Global Ocean-Atmosphere Coupled GCM (MRI-*

- CGCM2) and its climate sensitivity. Center for Global Environmental Research (CGER) Supercomputer Activity Report, National Institute for Environmental Studies, 10-2001, CGER-I054-2002.
- Zhao, L., Jin, H., Li, C., Cui, Z., Chang, X., Marchenko, S. S., Vandenberghe, J., Zhang, T., Luo, D., Guo, D., Liu, G. & Yi, C. 2014: The extent of permafrost in China during the local Last Glacial Maximum (LLGM). *Boreas* 43, 688–698.
- Zhang, T., Barry, R. G., Knowles, K., Ling, F. & Armstrong, R. L. 2003: Distribution of seasonally and perennially frozen ground in the Northern Hemisphere. In Phillips, M., Springman, S. M. & Arenson, L. U. (eds.): *Proceedings of the Eighth International Conference on Permafrost*, 1289–1294. A. A. Balkema, Brookfield.
- Zhang, T., Frauenfeld, O. W., McCreight, J. & Barry, R. G. 2005: *Northern Hemisphere EASE-Grid annual freezing and thawing indices, 1901–2002*. National Snow and Ice Data Center/World Data Center for Glaciology. Digital Media, Boulder.